Fermilab Library
0 1160 0052430 0

SSC-SDE-14

SSC-SDE
SOLENOIDAL DETECTOR NOTES

HERMETICITY IN THREE CRYOGENIC CALORIMETER GEOMETRIES

M. Strovink, W.J. Womersley, G.E. Forden

FERMILAB-Conf-89/xxx
D0 Note 839

DRAFT 4/18/89

Hermeticity in Three Cryogenic Calorimeter Geometries *

M. Strovink
University of California, Berkeley / Fermilab

W.J. Womersley
University of Florida

G.E. Forden
State University of New York, Stony Brook

Abstract

We calculate the effect of cracks and dead material on resolution in three simplified cryogenic calorimeter geometries, using a crude approximation that neglects transverse shower spreading and considers only a small set of incident angles. For each dead region, we estimate the average unseen energy using a shower parametrization, and relate it to resolution broadening using a simple approximation that agrees with experimental data. Making reasonable and consistent assumptions on cryostat wall thicknesses, we find that the effects of cracks and dead material dominate the expected resolution in the region where separate "barrel" and "end" cryostats meet. This is particularly true for one geometry in which the end calorimeter caps the barrel and also protrudes into the hole within it. We also find that carefully designed auxiliary "crack filler" detectors can substantially reduce the loss of resolution in these areas.

* *Invited talks presented at the Workshop on Calorimetry for the Super Collider, University of Alabama, March 13–17 1989.*

1. Introduction

Impressive tools now exist both for the mechanical engineering of cryogenic calorimeters and for the simulation of their expected response, including the often major effects of cracks and dead material in particular regions. For example, in the D-Zero collider detector at Fermilab, upon which these authors' efforts usually are focused, the calorimeter geometry is painstakingly represented, and the electromagnetic and hadronic cascades are simulated in great detail, using an adaptation of the program GEANT [1]. Nevertheless, in the early stages of designing a new calorimeter, e.g. for use at the SSC, many variations are possible, including basic differences in geometry — too many to engineer and simulate so thoroughly. Our objective here is to examine idealized cryostats having representative cracks and dead material, but different geometries, in order to learn:

— What basic geometry will give the best hermeticity?

— How valuable are auxiliary "crack filler" detectors?

— Will the hermeticity of a reasonably optimized cryogenic calorimeter for a general-purpose SSC detector lie in a reasonable range?

2. Calorimeter Geometries

As a starting point, we consider the cryogenic calorimeter being designed by Martin Marietta Astronautics in collaboration with N. DiGiacomo, H. Gordon, and M. Marx [2]. It conforms to the spatial requirements set by the Large Solenoid Detector subgroup at the 1987 Berkeley SSC workshop: the calorimeter encloses a tracking volume 3.2 m in diameter by 8 m long while remaining within an 8.2 m diameter by 16 m long outer boundary. The magnet coil is assumed to remain outside. Following the SLD design, all cryostats are aluminum. In the central "barrel" calorimeter, the argon vessel is strengthened and the double layer of active modules is supported by four "washers" that divide the vessel into five "bays". The modules, with trapezoidal cross section, are stiffened by "strongbacks" at their outer radius. The primary dead material, then, is contained in the cylindrical double wall, the washers and strongbacks, and especially the thick flat double walls at the ends.

On either end of the barrel calorimeter, as presented at this Workshop, the Martin Marietta design places an end calorimeter which caps the barrel and also protrudes into the cylindrical volume that it encloses. (We have come to refer to this cantilevered protrusion as a "nose".) The nose geometry is therefore a hybrid of the "endcap" geometry, in which the end calorimeter caps and lies completely outside a (shortened) barrel, and the "endplug"

geometry, in which the end calorimeter plugs and lies entirely within a (lengthened) barrel. These are the three end calorimeter geometries that we have considered.

In the calculations presented below, we have made two major simplifying assumptions about the geometry. First, we have ignored all azimuthal cracks. Such cracks, while potentially important especially if projective, would not affect our comparative analysis of end calorimeter geometries because they would be present in any of them. Second, we have imagined all calorimeter subvolumes to consist of one of only two types of uniform material: live, with radiation length $X_0 = 6.1$ mm and interaction length $\lambda = 180$ mm, as in D-Zero's uranium modules; and dead, with $X_0 = 178$ mm and $\lambda = 788$ mm, as in half density aluminum. The aluminum is taken to have half rather than full density to allow for the effects of construction and thermal expansion tolerances, superinsulation volumes, module edge effects, and stay-clear regions.

For the purposes of hermeticity calculation, our simplified model of the Martin Marietta calorimeter is shown in Fig. 1(*a*). Within the calorimeter outline, the inner regions are live and the (connected) outer regions are dead. At first glance the dead material seems abundant, at least until one realizes that it has only 1/29 the radiation thickness of the live material per unit of space on the page. The aluminum thicknesses used, scaled to full density, are:

		(mm)	
Barrel cryostat			
	Cylindrical double window (total)	50	(46.5)
	Flat double end window (total)	125	(152.4)
	Washer	50	(50.8)
	Strongback	100	
End cryostats			
	Flat double end window (total)		
	— inside 1.6 m radius	75	
	— outside 1.6 m radius	125	
	Outer double shell (total)	50	
	Washer	50	
	Cylindrical strut	25	

The numbers in parentheses are some of the thicknesses that were assumed in the Martin Marietta design at the time of this Workshop. Thus our simplified model is representative of their analysis at that time.

Figures 1(b) and 1(c) show, respectively, our simplified models of the endcap and endplug geometries. In the endcap geometry, the barrel calorimeter is shortened to three (slightly longer) bays, while in the endplug geometry it is lengthened to seven bays. Wherever possible, the assumptions made with regard to aluminum thicknesses are identical to those made for the nose geometry. Then, even if future engineering work changes the absolute wall thicknesses, conclusions reached here about the relative hermeticity of the three geometries would be expected not to change as much.

All three figures show a beam hole consisting of a six degree cone projecting to the origin (it is assumed that one or more smaller-angle calorimeters lie further downstream). Again, because the problem would be common to all three end calorimeter geometries considered here, we have not considered the effect on hermeticity of any beam hole (see E. Wang's contribution [3]). Nevertheless, we cannot resist observing that double conical walls like those shown represent a big projective crack with lots of dead material. A non-projective (i.e. cylindrical) beam hole would improve the hermeticity while still protecting the central rapidity region from forward shower albedo. With a cylindrical beam hole, coverage out to pseudorapidity > 3 could be achieved by lengthening the end calorimeter so that it extends further downstream.

3. Calculational Methods

A simple quantity that is directly related to calorimeter hermeticity is the fraction of the energy of a shower that is dissipated in dead material and therefore undetected. Obviously, the granularity of the dead material is crucial: in any practical sampling calorimeter most of the material consists of plates that are not live. Here by "dead material" we refer to extra material, much thicker than one calorimeter plate, that is introduced by a geometrical feature such as a cryostat wall. To the extent that there is a plateau in the pseudorapidity of produced shower primaries, Raja [4] has shown that the average undetected transverse energy due to such a feature is proportional to the integral over pseudorapidity, azimuth, and shower depth of the average fractional energy lost by the shower in the dead material.

In a well calibrated experiment, however, for each region one will multiply the observed shower energy by a factor that corrects for the average undetected energy fraction. Then the remaining effect of the dead material will be to broaden the resolution. To estimate this effect quickly, we have made the simple assumption that the energy lost in each dead layer fluctuates with an rms equal to its mean. Then each dead layer contributes in quadrature to the fractional energy resolution a quantity equal to the fraction of the total shower energy lost in that layer. This simple assumption is not expected to be exact,

but it does agree reasonably well with experimental data both for electromagnetic and hadronic showers. These comparisons are presented in Appendix B. We evaluated the thicknesses of each live and dead layer by using a computer-aided drafting program to trace rays at constant polar angles (at intervals of one or two degrees). Such a procedure introduces into the calculations an otherwise unnecessary granularity on that angular scale, and also suppresses the homogenizing effects of transverse shower spreading. Had time permitted, we would have preferred to automate the ray tracing and calculate the live and dead layer thicknesses for a much larger number of angles. Setting the shower widths to zero exaggerates the imperfections in small regions of the calorimeter. This helps with diagnostics, but it makes peaks in the plot of resolution vs. pseudorapidity too tall and too narrow (though the area of those peaks is about right).

After determining the live and dead layer thicknesses, we used a shower parametrization equivalent to that of Bock et al. [5] to compute the average energy lost in each dead layer, separately for pion and electron induced showers. This parametrization is described in Appendix A. In addition to the contributions from dead layers described above, we took the fractional energy resolution to be the sum in quadrature of a constant term (0.003 for electromagnetic showers, 0.02 for hadronic) and a term varying inversely with the square root of the energy, having a coefficient 0.16 $\mathrm{GeV}^{1/2}$ for electromagnetic showers, 0.49 for hadronic. These numbers were taken from D-Zero test beam results [6].

Generally we found it convenient to consider separately the calorimeter performance for electron-induced and pion-induced showers, because the effect of cracks and dead material is very different for the two cases. To estimate the performance for jets, we approximate R_{jet}, the fractional energy resolution for the jet, as

$$R_{\mathrm{jet}}^2 \approx \int_0^1 dz D(z)\{zR_{\mathrm{part}}(z)\}^2,$$

where $R_{\mathrm{part}}(z)^2 = \frac{2}{3}R_{\mathrm{had}}(z)^2 + \frac{1}{3}R_{\mathrm{EM}}(z)^2$, R_{had} (R_{EM}) is the single-pion (single-electron) fractional energy resolution, $D(z)$ is the jet fragmentation function, and z is the fraction of the jet energy carried by a single particle.

4. Results

The calculated percentage of undetected energy due to cracks and dead material near the region in which the barrel and end calorimeters meet is shown vs. pseudorapidity in Fig. 2(a)–(d). Results from the three different end calorimeter geometries (nose, endcap

and endplug as in Fig. 1 (a), (b), and (c)) are superimposed and presented separately for showers initiated by pions and electrons of transverse energy $E_T = 10$ and 100 GeV.

The undetected energy is substantial. For the least favorable case (the nose geometry) the maximum undetected energy fraction for electromagnetic showers ranges from 18% at 100 GeV E_T to 36% at 10 GeV. These maxima occur near the polar angle (19°) where the ray enters and exits five double cryostat walls (about 7 X_0) before encountering a significant amount of live material. The maximum undetected energy for the more favorable geometries (endcap and endplug) is about a factor of three smaller. For hadronic showers, the nose geometry at worst fails to detect 14% of the energy at $E_T = 100$ GeV and 27% at 10 GeV, with a broader peak in the resolution again centered near 19°. The endcap and endplug geometries are a factor of 1.5 to 2 better.

The corresponding fractional energy resolutions are presented in Fig. 3(a)–(d). The superiority of the endcap and endplug over the nose geometry again is clear. At worst, the nose geometry is estimated to produce electromagnetic resolutions $\sim$ one order of magnitude worse, and hadronic resolutions $\sim$ one-half order of magnitude worse, than can be achieved away from the regions having substantial cracks and dead material. From the localized nature of the resolution peaks, especially for electromagnetic showers, it seems that once the undetected energy fraction drops below a threshold, the performance is little different from ideal.

The estimated fractional energy resolution for $E_T = 100$ and 1000 GeV jets is shown for the three geometries in Fig. 4(a)–(b). The jet resolutions follow the general trend expected for a mixture of hadronic and electromagnetic single-particle resolutions.

5. Crack Fillers

Given the existence of a layer of dead material, it is obvious that extra information would be obtained by sampling the shower part way through it. That sample is correlated with the shower energy lost in the dead layer, making possible a correction that varies shower by shower. This is the function of the "crack filler" detectors being constructed for use near the interface of D-Zero's barrel and end calorimeters. Detailed GEANT simulations [7] show that they substantially improve the missing energy performance in that region.

How might such improvement be estimated quickly? Consider the elementary case in which a dead layer is split into two thinner layers with equal average shower energy loss. If we apply our simple approximation, described above, relating undetected energy

to resolution broadening, the total contribution in quadrature of that dead layer to the resolution would be reduced by a factor of $\sqrt{2}$. Qualitatively this is not unreasonable since new information would be added by the crack filler detector between the two layers.

However, in the calculations presented here, we decided instead to consider crack fillers consisting not of a single sampling plane, but rather of a piece of live calorimeter thick enough to absorb most of an electromagnetic shower. We made this choice primarily because our simple relation between undetected energy and resolution broadening would seem more reliable if correlations between shower fluctuations in nearby dead layers could be reduced. Also, in some geometries, a thicker crack filler would push dead material to greater shower depths where the average undetected energy might be less.

Physically, we imagine a crack filler to consist of a 15–25 cm thick "crackless" layer of live calorimeter with the same average X_0 and λ as the main calorimeter, supported by a 10 cm thick dead layer of half density aluminum. Compared to the main calorimeter, it should also have similar critical energy, integration time, and neutron absorption and hadron/electron compensation characteristics. Possible technologies would include Si with Pb/Fe or U plates; Pb-scintillator in various forms; or UA1-style TMP boxes with Pb or U plates. To reduce cracks, these boxes should have thicker skins to avoid the need for clamping, and should not include TMP manifolds.

In our first attempt at adding crack fillers, we put them upstream of all regions of the barrel and end calorimeters containing larger than usual cryostat wall thicknesses. The peaks in electron shower resolution vs. pseudorapidity were largely removed, but in broad regions the hadron shower resolution was made worse. This occurred because the inclusion of crack filler material moved the cryostat material to a greater hadron shower depth, increasing the average energy loss in it. Also, occasionally a ray traversed a few X_0 of the corner of a crack detector, moving cryostat material near electromagnetic shower maximum. This produced new isolated peaks in the plot of electron shower resolution vs. pseudorapidity.

From this initial failure we conclude:

— Crack fillers usually should not be added as the first material encountered by shower primaries. For pion-initiated showers, if a certain amount of dead material must be present, it is best to keep it at the front where the energy lost in it is minimized.

— Corners of live calorimeter material should be projectively beveled so that the amount of live material encountered either is enough to absorb most of an electromagnetic shower, or is zero.

A corollary is that, for pion-initiated showers, it is better to put a magnet coil inside the whole calorimeter rather than between its electromgnetic and hadronic sections.

Our second attempt to add crack fillers is shown for the three geometries in Fig. 5(a)–(c). For clarity the live part of the crack filler is shaded and the dead part is blackened. The calculated resolution, in the same format as without crack fillers in Fig. 3, is presented in Fig. 6(a)–(d). It is evident that the peaks in electromagnetic shower resolution have nearly vanished. The narrow peak for the endcap geometry at electron pseudorapidity near 1.4 is an artifact due to a particular ray clipping the corner of a live region of the main calorimeter, which had not been properly beveled. In Fig. 5the broader peaks in the pion shower resolution generally are reduced by factor of 1.5 to 3 when compared to Fig. 3. Although much more optimization remains to be done, we view this second attempt as a successful application of crack fillers to the cryogenic hermeticity problem.

6. Conclusions

For the cryostats considered here (aluminum construction, realistic wall thicknesses, flat end walls, magnet coil outside) the effects of cracks and dead material between barrel and end calorimeters are serious for electron-induced showers (without crack fillers) and also for pion-induced showers. By "serious" we mean that there are sizable rapidity intervals (up to ~ 1 unit in total) in which the resolution is at least doubled. We do not address the issue of the effect of this degradation on measurement of physics processes. However, it is clear that for cryogenic calorimeters, cracks and dead material play an important role in defining the level of resolution for which it is reasonable to strive.

Without crack fillers, we find the endcap and endplug geometries to be comparable in the effects of cracks and dead material on resolution; the nose geometry is significantly worse.

If "crack filler" detectors are to be used, they must be carefully designed and incorporated into the cryostat geometry from the outset. At the expense of additional complexity and inhomogeneity, such detectors can be expected to largely remove the barrel-end calorimeter interface problem for electron-induced showers, and to give moderate improvement for pion-induced showers.

It is obvious to us that many more and better hermeticity calculations remain to be done. It is important to do them soon, before various detailed calorimeter designs acquire a life of their own. In the short run, we do not necessarily need the power of GEANT. What would help greatly would be the marriage of a computer-aided drafting program with a

geometry program that would automatically calculate thicknesses of live and dead layers. Such a system, based on the techniques we have described in this paper, is indeed being implemented by Martin Marietta for use in the further development of their calorimeter design.

Appendix A — Shower Parametrizations

The form of the parametrizations used to calculate the average energy deposition as a function of distance through the detector, s, was as follows. For electromagnetic showers:

$$dE = E\frac{x^{a-1}e^{-x}}{\Gamma(a)}dx$$

where $x = bs/X_0$, $a = 2.4215 + 0.4847\ln E$ and $b = 0.4250$.

For hadronic showers:

$$dE = E\{w\frac{y^{\alpha_E-1}e^{-y}}{\Gamma(\alpha_E)}dy + (1-w)\frac{z^{\alpha_H-1}e^{-z}}{\Gamma(\alpha_H)}dz\}$$

where $y = \beta_E(s-s_0)/X_0$, $z = \beta_H(s-s_0)/\lambda$, $\alpha_E = \alpha_H = 0.6165+0.3183\ln E$, $\beta_E = 0.2198$, $\beta_H = 0.9099 - 0.0237\ln E$, $w = 0.4634$, and s_0 is the coordinate of the start of the shower which is generated randomly according to $e^{-s_0/\lambda}$.

Appendix B — Effect of Undetected Energy on Resolution

The parametrization was used to calculate the mean energy deposited in each layer of the calorimeter, live or dead. We then made the ansatz that provided the mean energy $\langle E_d\rangle$ deposited in a layer of dead material was small compared to the incident energy E, E_d was distributed with a variance $\sigma_d^2 \sim \langle E_d\rangle^2$. The fluctuations of E_d lead to a degradation of the fractional energy resolution R, which becomes:

$$R = \left(R_0^2 + \Sigma_{\text{Dead layers}}\left(\frac{E_d}{E}\right)^2\right)^{1/2}$$

where R_0 is the fractional resolution obtained without any dead material. The incoherent sum over dead layers assumes, of course, that the energies in the various dead parts of the detector are uncorrelated: this is reasonable if they are an interaction length or more apart. We took $R_0^2 = 0.16^2/E + 0.003^2$ for electromagnetic showers and $R_0^2 = 0.49^2/E + 0.02^2$ for hadronic, based on D-Zero test beam results [6].

The ansatz is not unreasonable: $\sigma_d^2 = \langle E_d \rangle^2$ is rigorously true (in the limit of large mul tiplicity) for thin layers of material in an electromagnetic shower evolving according to a Furry distribution [9]. The major justification for this ansatz however lies in its success. The following situations have been tested:

— 50 GeV test beam electrons incident on a D-Zero central calorimeter electromagnetic module. If the first layer (2 X_0), or the first two layers (4 X_0) of the calorimeter are switched off, this technique successfully predicts the worsening of resolution.

— H1 results on the effect of adding an aluminum dead layer upstream of a lead-argon electromagnetic calorimeter module [8]. This technique successfully predicts the worsening of resolution for 1–3 X_0 of aluminum, for electrons from 1 to 35 GeV.

— 25 to 150 GeV test beam pions incident on a D-Zero end calorimeter hadronic module. If the first layer (1 λ), or the last layer (from 4 λ to 8 λ) of the calorimeter are switched off, this technique successfully predicts the worsening of resolution.

References

[1] R. Brun *et al.*, GEANT3 Users' Guide, CERN DD/EE/84-1, May 1986.

A.M. Jonckheere, D0GEANT Users' Guide.

[2] N. DiGiacomo *et al.*, these proceedings.

We thank M. Marx for making aspects of this design available to us prior to the Workshop.

[3] E. Wang, these proceedings.

[4] R. Raja, D0 Internal Note 461 (1986).

[5] R.K. Bock, T. Hansl-Kozanecka, and T.P. Shah, Nucl. Instr. & Meth. 186 (1981) 533.

We thank T. Hansl-Kozanecka for the use of her subroutine to evaluate this parametrization.

[6] D0 Calorimeter Group (M. Abolins *et al.*), Fermilab-Pub-89/38-E, to be published in Nucl. Instr. & Methods A (1989).

[7] A.P. White, D0 Internal Note 769 (1988)

[8] G. Cozzika, in Proceedings of Workshop for the Comparative Engineering Study of Cryostat Systems for Generic Hermetic Liquid Argon Calorimeters for the SSC, University of Colorado, December 1988.

[9] F.W. Furry, Phys. Rev. 52 (1937) 569.

Figure Captions

Figure 1

(a) Our simplified model of the Martin Mar ietta calorimeter design (Ref. [2]); (b) our simplified endcap, and (c) endplug, calorimeter designs.

Figure 2

Percentages of incident particle energy deposited in dead material near the region in which the barrel and end calorimeters meet.

Results from the three different end calorimeter geometries (nose, endcap and endplug as in Fig. 1 (a), (b), and (c)) are superimposed for showers initiated by (a) pions of transverse energy $E_T = 10$ GeV, (b) electrons of $E_T = 10$ GeV, (c) pions of $E_T = 10$) GeV, and (d) electrons of $E_T = 100$ GeV.

Figure 3

Fractional energy resolutions for single particles, for the three different end calorimeter geometries (nose, endcap and endplug as in Fig. 1 (a), (b), and (c)).

Shown are results for (a) pions of transverse energy $E_T = 10$ GeV, (b) electrons of $E_T = 10$ GeV, (c) pions of $E_T = 100$ GeV, and (d) electrons of $E_T = 100$ GeV.

Figure 4

Fractional jet energy resolutions, for the three different end calorimeter geometries (nose, endcap and endplug as in Fig. 1 (a), (b), and (c)). Shown are results for jets of transverse energy E_T equal to (a) 100 GeV and (b) 1000 GeV.

Figure 5

Our simple models of calorimeter designs after the addition of "crack fillers": (a) the Martin Mar ietta calorimeter design; (b) endcap, and (c) endplug. The live part of the crack filler detectors is shaded and the dead parts (supports) are blackened.

Figure 6

Fractional energy resolutions for single particles, for the three different end calorimeter geometries with crack fillers (nose, endcap and endplug as in Fig. 5 (a), (b), and (c)).

Shown are results for (a) pions of transverse energy $E_T = 10$ GeV, (b) electrons of $E_T = 10$ GeV, (c) pions of $E_T = 100$ GeV, and (d) electrons of $E_T = 100$ GeV.

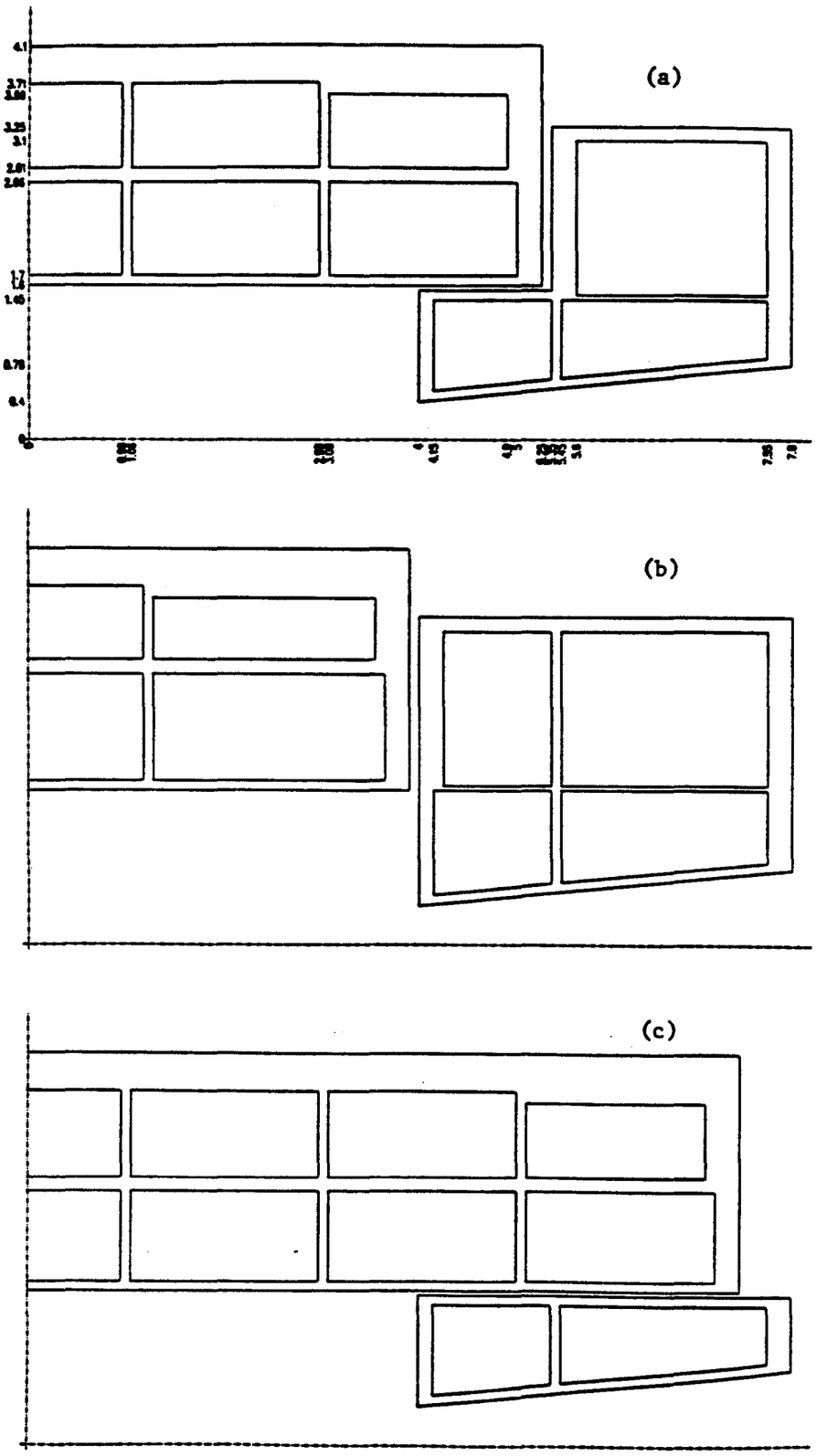

Fig. 1

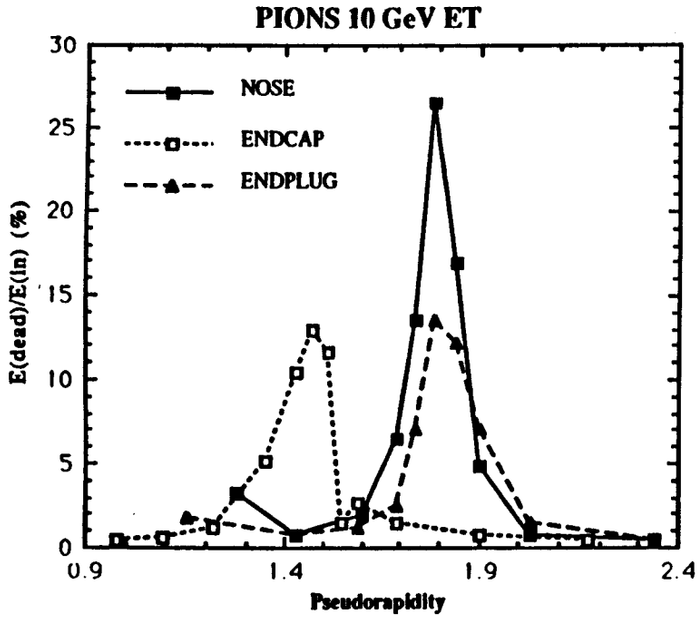
PIONS 10 GeV ET
NOSE
ENDCAP
ENDPLUG
E(dead)/E(in) (%)
Pseudorapidity
0
5
10
15
20
25
30
0.9
1.4
1.9
2.4

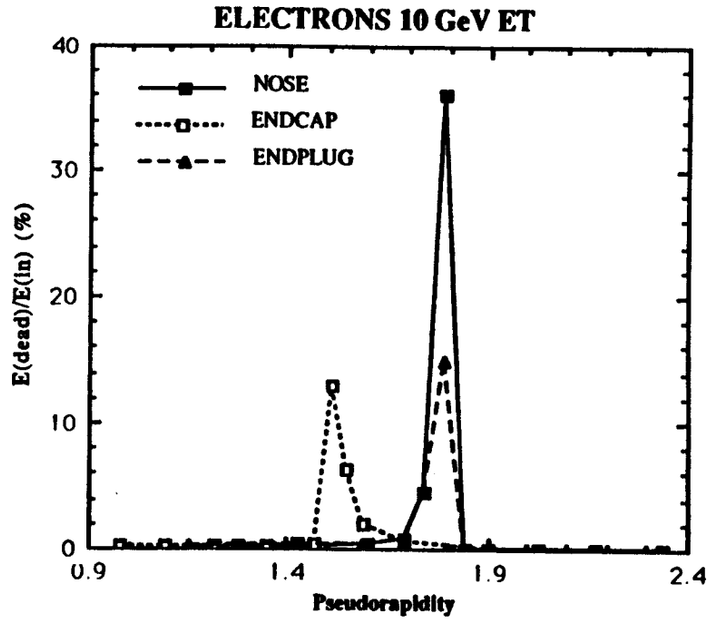
ELECTRONS 10 GeV ET
NOSE
ENDCAP
ENDPLUG
E(dead)/E(in) (%)
Pseudorapidity
0
10
20
30
40
0.9
1.4
1.9
2.4

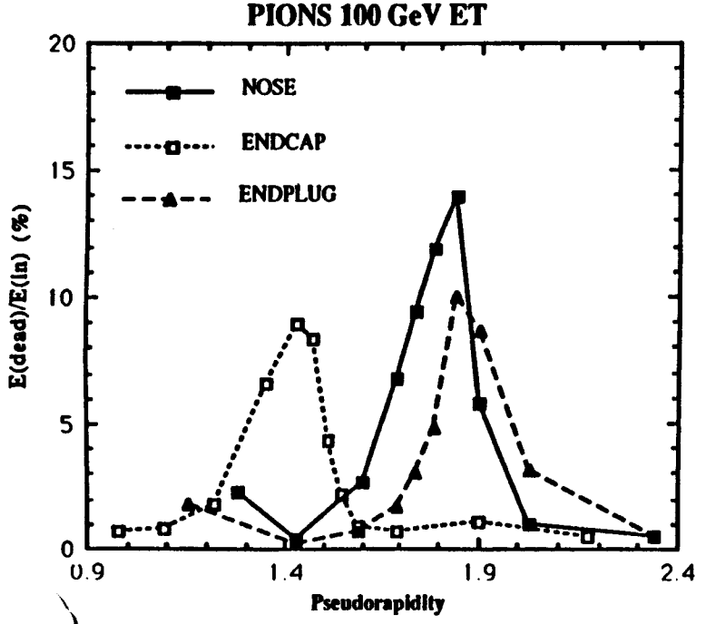
PIONS 100 GeV ET
NOSE
ENDCAP
ENDPLUG
E(dead)/E(in) (%)
Pseudorapidity
0
5
10
15
20
0.9
1.4
1.9
2.4

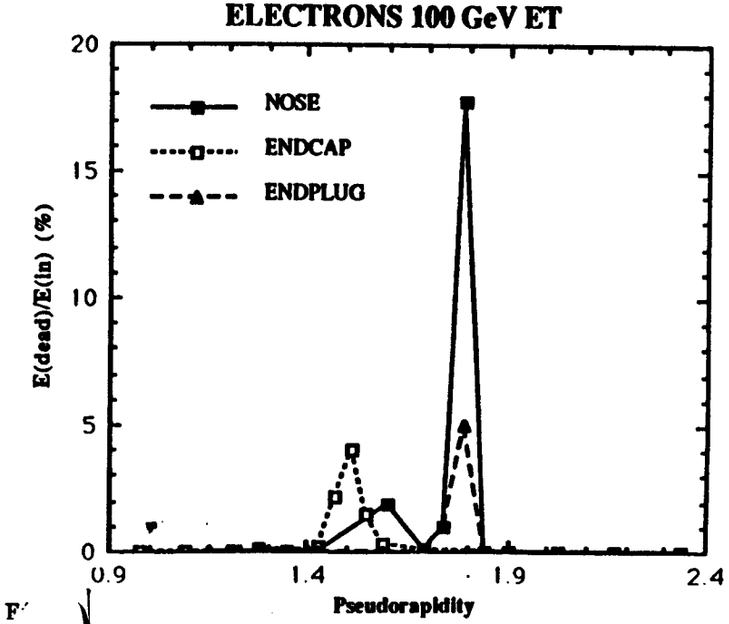
ELECTRONS 100 GeV ET
NOSE
ENDCAP
ENDPLUG
E(dead)/E(in) (%)
Pseudorapidity
0
5
10
15
20
0.9
1.4
1.9
2.4

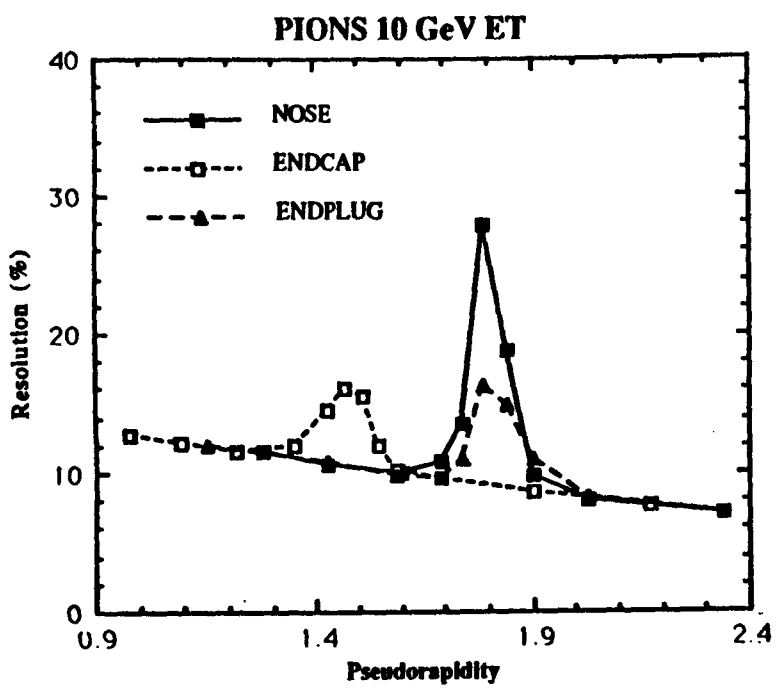
PIONS 10 GeV ET
NOSE
ENDCAP
ENDPLUG
Resolution (%)
Pseudorapidity
0
10
20
30
0.9
1.4
1.9
2.4

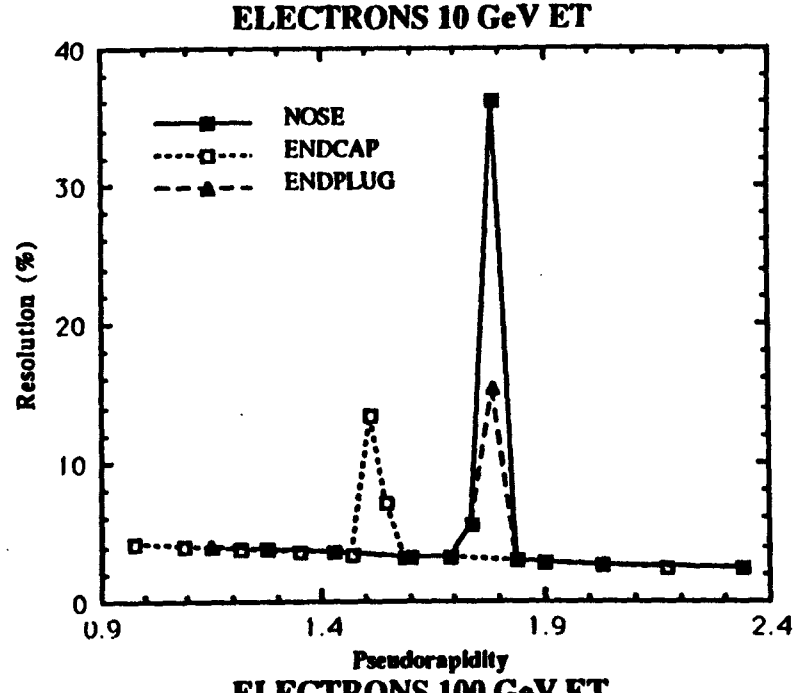
ELECTRONS 10 GeV ET
NOSE
ENDCAP
ENDPLUG
Resolution (%)
Pseudorapidity
0
10
20
30
0.9
1.4
1.9
2.4

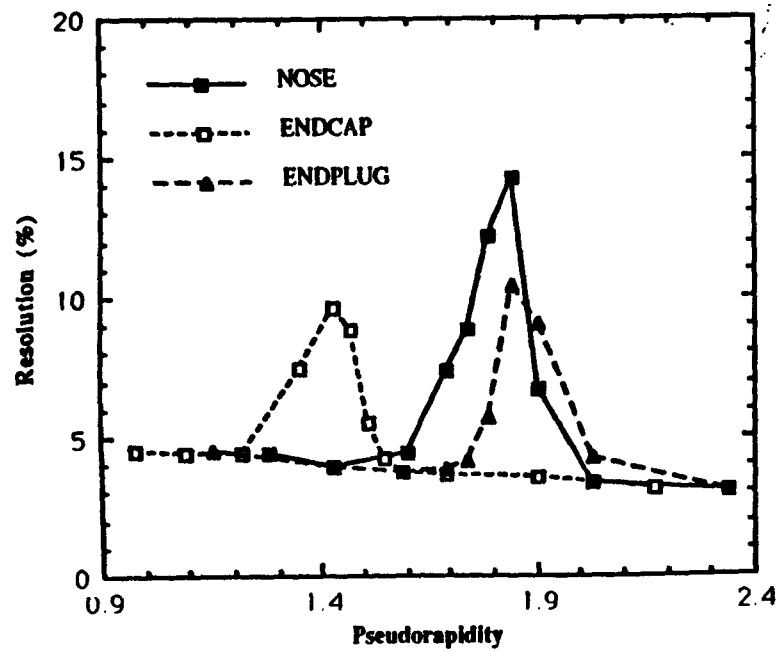
PIONS 100 GeV ET
NOSE
ENDCAP
ENDPLUG
Resolution (%)
Pseudorapidity
0
5
10
15
20
0.9
1.4
1.9
2.4

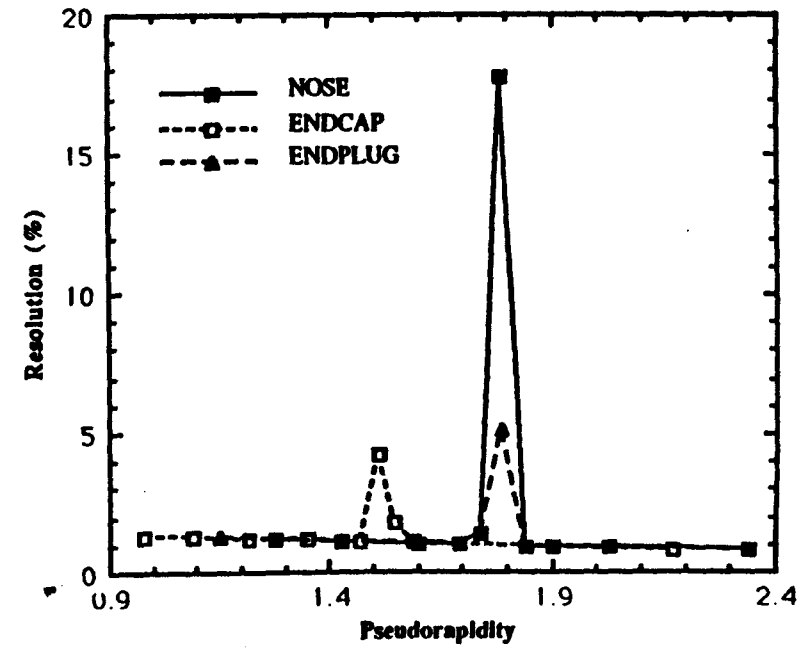
ELECTRONS 100 GeV ET
NOSE
ENDCAP
ENDPLUG
Resolution (%)
Pseudorapidity
0
5
10
15
20
0.9
1.4
1.9
2.4

Fig. 3

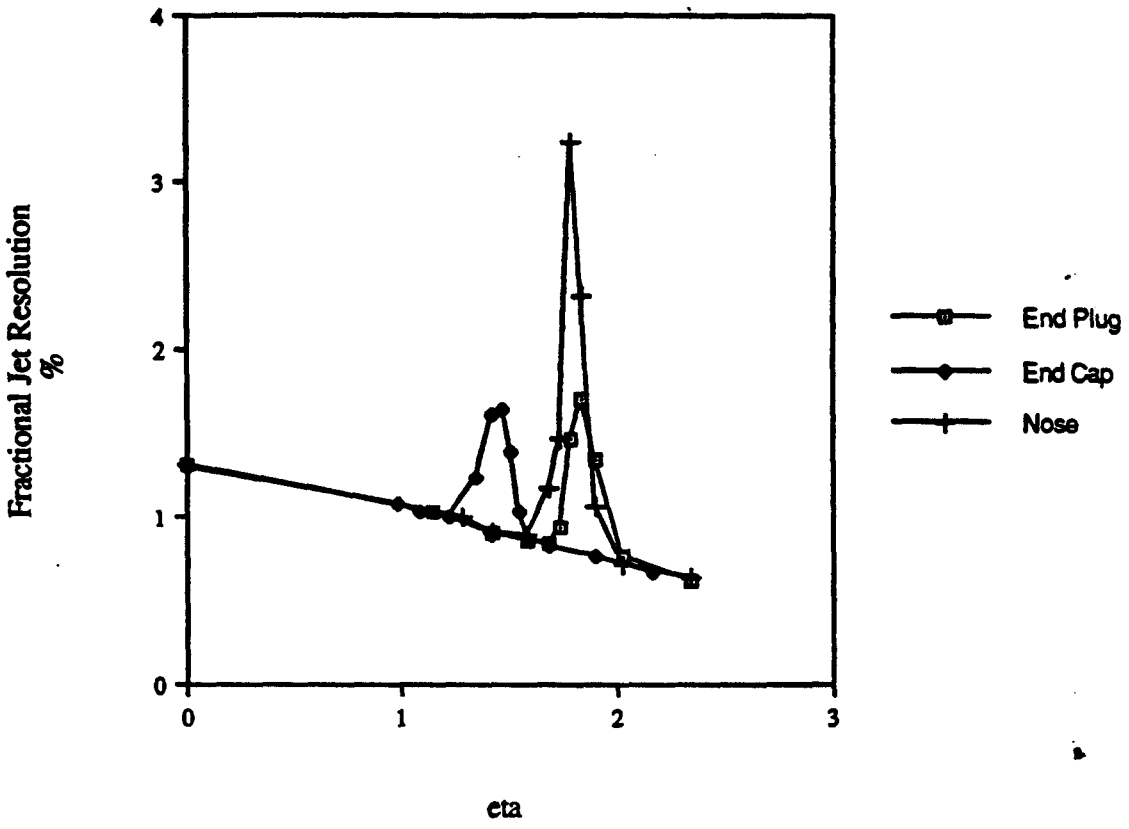
1000 GeV Jet Et
Fractional Jet Resolution %
4
3
2
1
0
0
1
2
3
eta
End Plug
End Cap
Nose

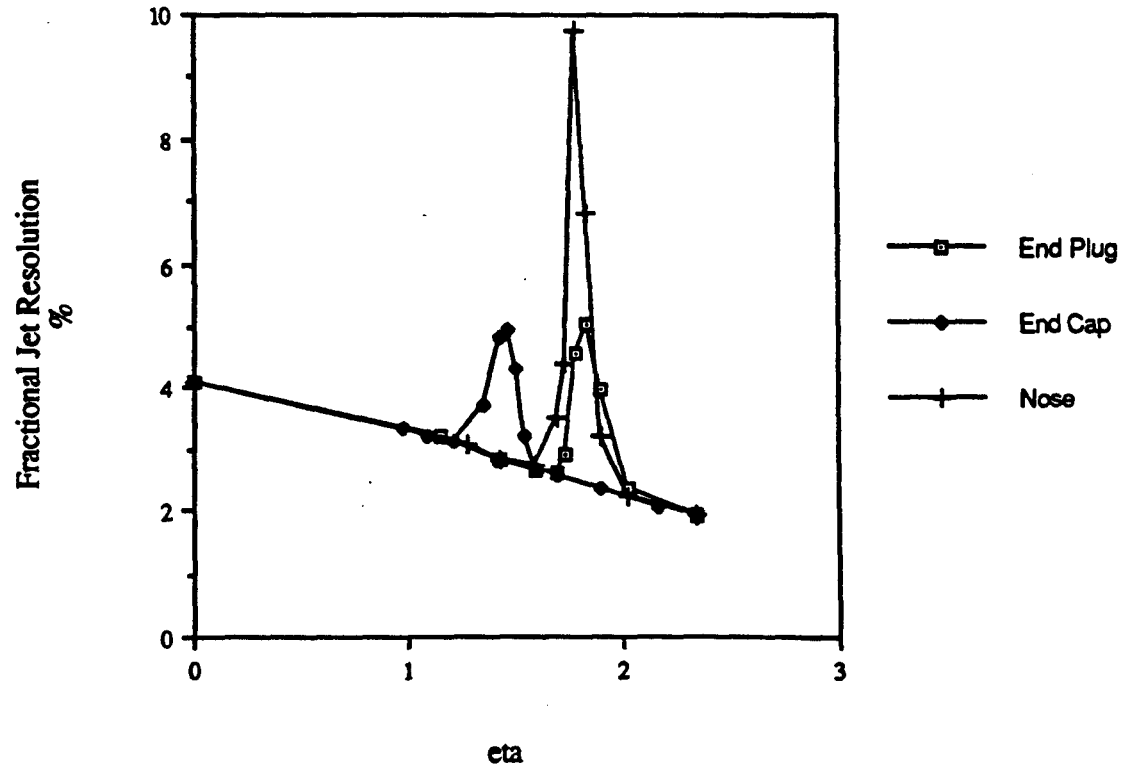
100 GeV Jet Et
Fractional Jet Resolution %
10
8
6
4
2
0
0
1
2
3
eta
End Plug
End Cap
Nose

Fig. 4

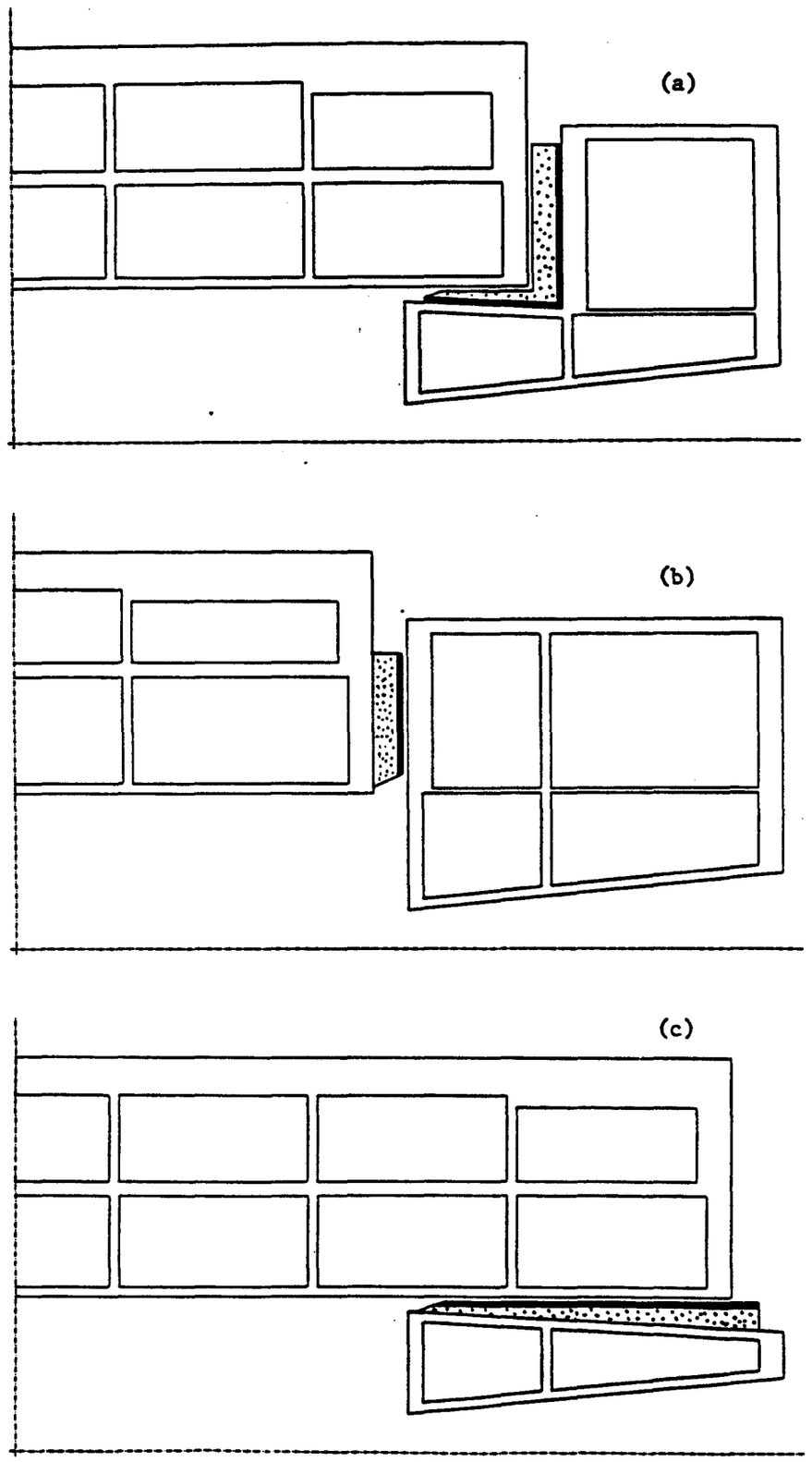

Fig. 5

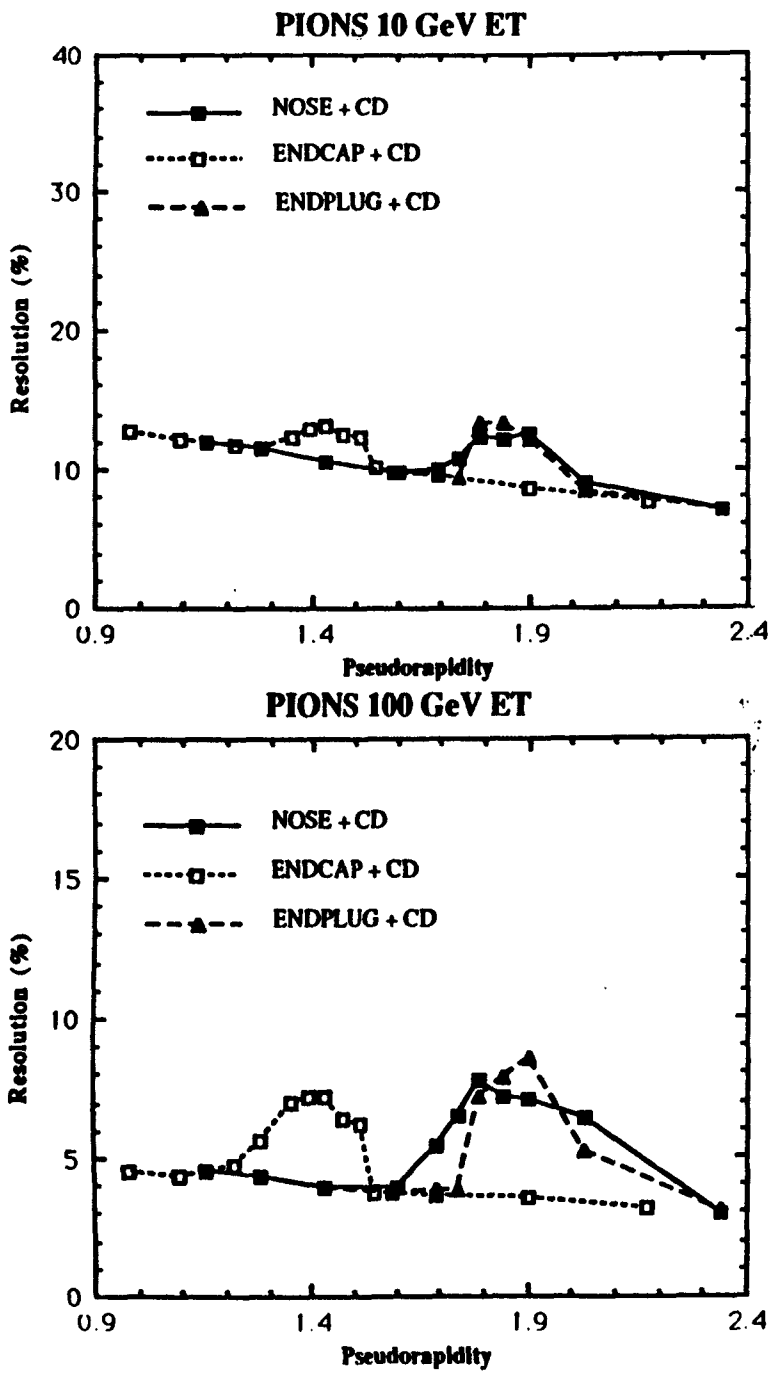
PIONS 10 GeV ET
NOSE + CD
ENDCAP + CD
ENDPLUG + CD
Resolution (%)
Pseudorapidity
PIONS 100 GeV ET
NOSE + CD
ENDCAP + CD
ENDPLUG + CD
Resolution (%)
Pseudorapidity

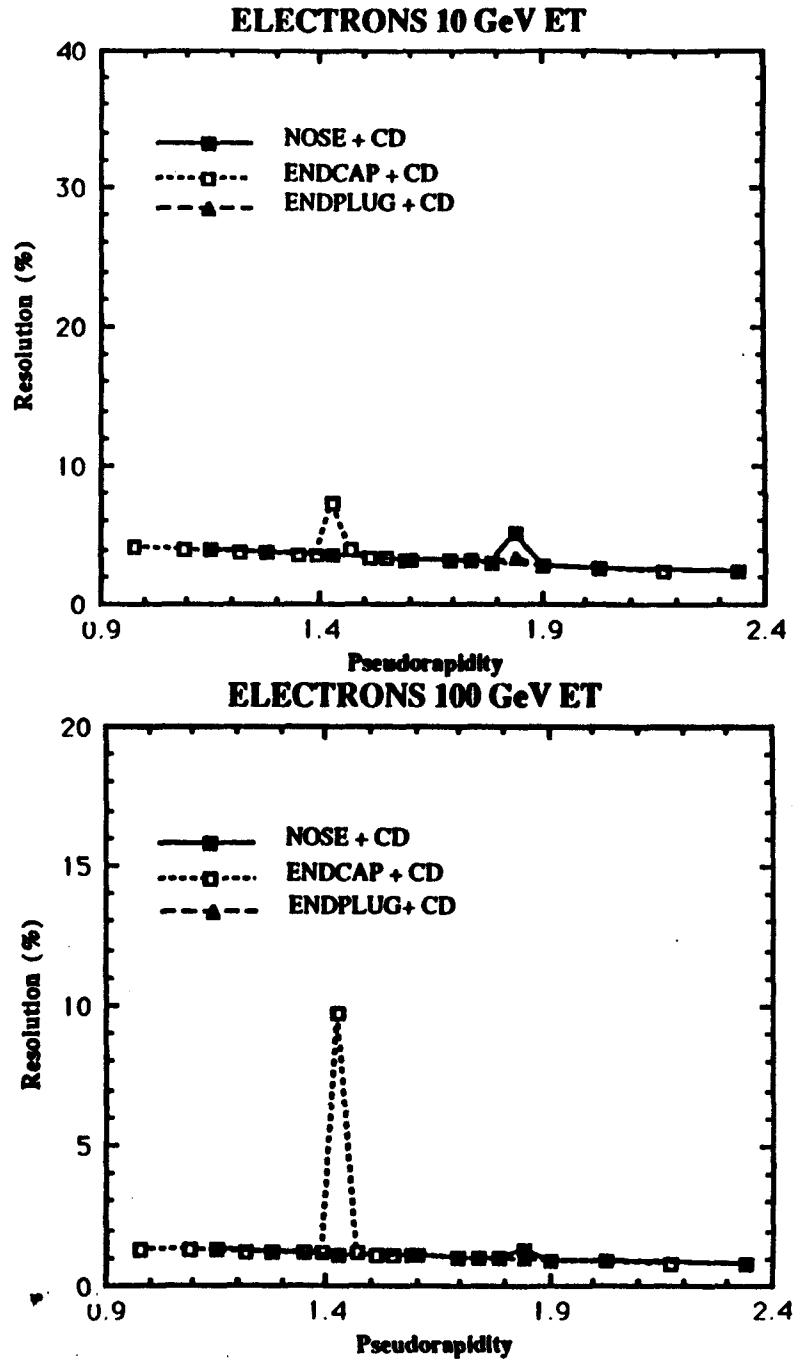
ELECTRONS 10 GeV ET
NOSE + CD
ENDCAP + CD
ENDPLUG + CD
Resolution (%)
Pseudorapidity
ELECTRONS 100 GeV ET
NOSE + CD
ENDCAP + CD
ENDPLUG+ CD
Resolution (%)
Pseudorapidity

Fig